EDGE ARTICLE

Check for updates

All publication charges for this article have been paid for by the Royal Society of Chemistry

Mn²⁺-induced structural flexibility enhances the entire catalytic cycle and the cleavage of mismatches in prokaryotic argonaute proteins†

Lirong Zheng, ‡[ae] Bingxin Zhou,‡*[ac] Yu Yang,‡[b] Bing Zan,‡[a] Bozitao Zhong, [b] Banghao Wu,[b] Yan Feng,[b] Qian Liu*[b] and Liang Hong*[abcd]

Prokaryotic Argonaute (pAgo) proteins, a class of DNA/RNA-guided programmable endonucleases, have been extensively utilized in nucleic acid-based biosensors. The specific binding and cleavage of nucleic acids by pAgo proteins, which are crucial processes for their applications, are dependent on the presence of Mn²⁺ bound in the pockets, as verified through X-ray crystallography. However, a comprehensive understanding of how dissociated Mn²⁺ in the solvent affects the catalytic cycle, and its underlying regulatory role in this structure–function relationship, remains underdetermined. By combining experimental and computational methods, this study reveals that unbound Mn²⁺ in solution enhances the flexibility of diverse pAgo proteins. This increase in flexibility through decreasing the number of hydrogen bonds, induced by Mn²⁺, leads to higher affinity for substrates, thus facilitating cleavage. More importantly, Mn²⁺-induced structural flexibility increases the mismatch tolerance between guide-target pairs by increasing the conformational states, thereby enhancing the cleavage of mismatches. Further simulations indicate that the enhanced flexibility in linkers triggers conformational changes in the PAZ domain for recognizing various lengths of nucleic acids. Additionally, Mn²⁺-induced dynamic alterations of the protein cause a conformational shift in the N domain and catalytic sites towards their functional form, resulting in a decreased energy penalty for target release and cleavage. These findings demonstrate that the dynamic conformations of pAgo proteins, resulting from the presence of the unbound Mn²⁺ in solution, significantly promote the catalytic cycle of endonucleases and the tolerance of cleavage to mismatches. This flexibility enhancement mechanism serves as a general strategy employed by Ago proteins from diverse prokaryotes to accomplish their catalytic functions and provide useful information for Ago-based precise molecular diagnostics.

Introduction

Prokaryotic Argonaute (pAgo) proteins, a class of endonucleases that play a crucial role in DNA interference in prokaryotic organisms,[1–3] have gained significant attention in the field of biotechnology and medicine for their ability to target and cleave specific sequences in DNA/RNA.[4–11] One of the most important applications is diagnostics, where pAgo proteins can be utilized to design molecular diagnostic assays that detect and quantify specific nucleic acid sequences, such as pathogens or cancer-associated mutations.[6,7,12–14] These assays lead to the development of more sensitive and specific diagnostic methods, greatly improving the early detection and accurate treatment of diseases. Another crucial use of pAgo proteins is to label nucleic acids both *in vitro* and *in vivo*.[15–18] Their high affinity to the substrate, stability in the protein-substrate complex, and specific recognition of the target sequence offer significant advantages over traditional methods that rely on nucleic acid binding, such as DNA-painting and DNA fluorescence *in situ* hybridization (FISH) technology. Furthermore, the combined action of pAgo proteins and nuclease-deficient RecBC helicase can cleave double-strand DNA,[10] potentially leading to the design of gene therapies that specifically target disease-causing genes. These applications of pAgo proteins provide new possibilities for the development of therapeutics and genetic manipulation technologies.

[a]Institute of Natural Sciences, Shanghai Jiao Tong University, Shanghai 200240, China. E-mail: hongl3liang@sjtu.edu.cn; bingxin.zhou@sjtu.edu.cn

[b]State Key Laboratory for Microbial Metabolism, School of Life Sciences and Biotechnology, Shanghai Jiao Tong University, Shanghai 200240, China. E-mail: liuqian1018@sjtu.edu.cn

[c]Shanghai National Center for Applied Mathematics (SJTU Center), Shanghai Jiao Tong University, Shanghai 200240, China

[d]Zhangjiang Institute for Advanced Study, Shanghai Jiao Tong University, Shanghai 200240, China

[e]Department of Cell and Developmental Biology & Michigan Neuroscience Institute, University of Michigan Medical School, 48105, Ann Arbor, MI, USA

pAgo proteins predominantly contain six domains, including the N-terminal domain, Linker1, PIWI-Argonaute-Zwille domain (PAZ), Linker2, middle domain (MID), and P-element Induced Wimpy Testis domain (PIWI).[3,19,20] Notably, the structural dynamics of these domains are critical for the biofunction of pAgo proteins.[21–26] The pAgo proteins bind to guide nucleic acids, with the 5′-end and 3′-end of the nucleic acid being accommodated in the basic pocket of the MID domain and the PAZ domain, respectively.[27] This guide-loaded complex then searches for complementary target strands through base-pairing with the seed region of the guide strand, which is followed by the propagation of the nucleic acid duplex.[21,27] Subsequently, the 3′-end of the guide is released from the PAZ domain, and the active site of the Glu-finger is closed for the correct base-pairing.[21] Conformational changes of the catalytic tetrad in the PIWI domain then allow for the cleavage of the target strand.[21] Finally, the N domain helps to release the cleaved target, and the protein–guide complex is rearranged to its initial conformation for the next round of cleavage.[28,29]

In particular, the presence of Mn^{2+} is crucial for the catalytic activity of pAgo proteins, as determined by their crystal structures.[21,25,30–34] Most known pAgo proteins utilize one Mn^{2+} bound to the MID pocket for interactions with the 5′ phosphate in the guide strand, and two Mn^{2+} ions bound to the catalytic sites (a DEDX motif, where X is K, D, or H) in the PIWI domain for cleavage of the target strand between the 10th and 11th bases, counted from the 5′-end of the guide.[21,31] Despite the direct role of these bound Mn^{2+}, a large number of Mn^{2+} are dissociated and present in the solvent. However, the role of these free ions in the catalytic function of pAgo proteins remains unknown. This situation prompts the question of whether these unbound Mn^{2+} in the solvent affect the functional flexibility of pAgo proteins and, subsequently, influence the endonuclease activity of pAgo proteins.

In this study, we employed a combination of differential scanning fluorimetry (DSF), nano differential scanning calorimetry (nano DSC), circular dichroism (CD) spectrum, synchrotron small-angle X-ray scattering (SAXS), biochemical assays, and molecular dynamics (MD) simulation to investigate the impact of unbound Mn^{2+} on the structural dynamics and endonuclease activity of prokaryotic Argonaute (pAgo) proteins from mesophilic (*Clostridium butyricum* Ago (*Cb*Ago),[31] *Paenibacilllus borealis* Ago (*Pb*Ago),[35] *Pseudooceanicola lipolyticus* Ago (*Pli*Ago),[30] and *Brevibacillus laterosporus* Ago (*Bl*Ago)[35]), thermophilic (*Thermus thermophilus* Ago (*Tt*Ago)) and hyperthermophilic (*Pyrococcus furiosus* Ago (*Pf*Ago),[36] *Methanocaldococcus fervens* Ago (*Mf*Ago)[37] and *Ferroglobus placidus* Ago (*Fp*Ago)[38]) organisms. Our results indicate that the presence of unbound Mn^{2+} reduces the hydrogen bonds in pAgo proteins from mesophiles to hyperthermophiles. This reduction in hydrogen bonds grants the protein a large degree of structural flexibility, while the overall packing of the protein remains intact. Furthermore, we demonstrated that Mn^{2+}-dependent dynamics of pAgo proteins show a higher affinity to substrates and thus greatly promote the binding between the guide and target strands, which is key to facilitating the cleavage activity.

Remarkably, Mn^{2+} exerts a significant influence on the precision of target DNA cleavage, which increases mismatch tolerance between guide–target pairs by increasing the conformational states. All-atom MD simulations at the conditions mimicking the Mn^{2+}-present solvent environment revealed that the flexibility of Link 1 and Link 2 is greatly enhanced after incubating with Mn^{2+}, which induces the conformational change of the PAZ domain to recognize various lengths of guide strands. Additionally, the increased flexibility in the glue-finger and the PAZ domain could help the propagation of duplexes. Furthermore, the Mn^{2+}-induced dynamical change shifts the conformation of catalytic sites and the N domain towards its functional form, lowering the energy penalty for target strand cleavage and release, respectively. Overall, our data revealed that the unbound Mn^{2+}-induced flexibility of pAgo proteins is crucial for their catalytic functions, and these findings are generally valid for pAgo proteins obtained from various prokaryotes. Moreover, this study sheds light on the underlying molecular mechanisms of the catalytic cycle of pAgo proteins, providing new avenues for research in the field of prokaryotic immunity systems and precise molecular diagnostics.

Results

Mn^{2+} enhances the flexibility of pAgo proteins obtained from mesophiles, thermophiles, and hyperthermophiles.

The molecular architecture of long pAgo protein is characterized by a distinct two-lobed structure, which is a common feature among members of this family[3,22] (Fig. 1A). The first lobe comprises the N domain, Linker 1, and PAZ domain, while the second lobe comprises the Linker 2, MID domain, and PIWI domain (Fig. 1B). The phylogenetic position of pAgo proteins studied herein, as well as their structural characteristics, are presented in Fig. 1C and S1,† respectively. Although the overall packing topology of pAgo proteins obtained from different prokaryotes exhibits a similar tertiary and secondary structure, their functions and optimal physiological temperatures are vastly divergent.[3,24]

We first examined how the secondary structures of pAgo proteins vary with the concentration of Mn^{2+} at their respective physiological temperatures. We used CD spectroscopy, a technique that measures the secondary structure of a protein by analyzing its absorption of the circularly polarized light.[39] The results indicate that the presence of Mn^{2+} does not significantly alter the secondary structures of pAgo proteins (Fig. S2A–C†). It should be noted that we use Mn^{2+} in this study rather than Mg^{2+} because *Pf*Ago cannot perform its functions when using Mg^{2+}.[36]

We then characterized the effect of Mn^{2+} on the thermostability of pAgo proteins by using DSF spectroscopy. The DSF method is a quantitative method that allows for the assessment of thermostability by measuring changes in fluorescence intensity as the temperature is progressively increased, which monitors the tertiary structural changes in proteins.[40] The melting temperature (T_m) of the tertiary structure of different pAgo proteins was determined with and without the presence of Mn^{2+}. As shown in Fig. 1D–J, the addition of Mn^{2+} results in
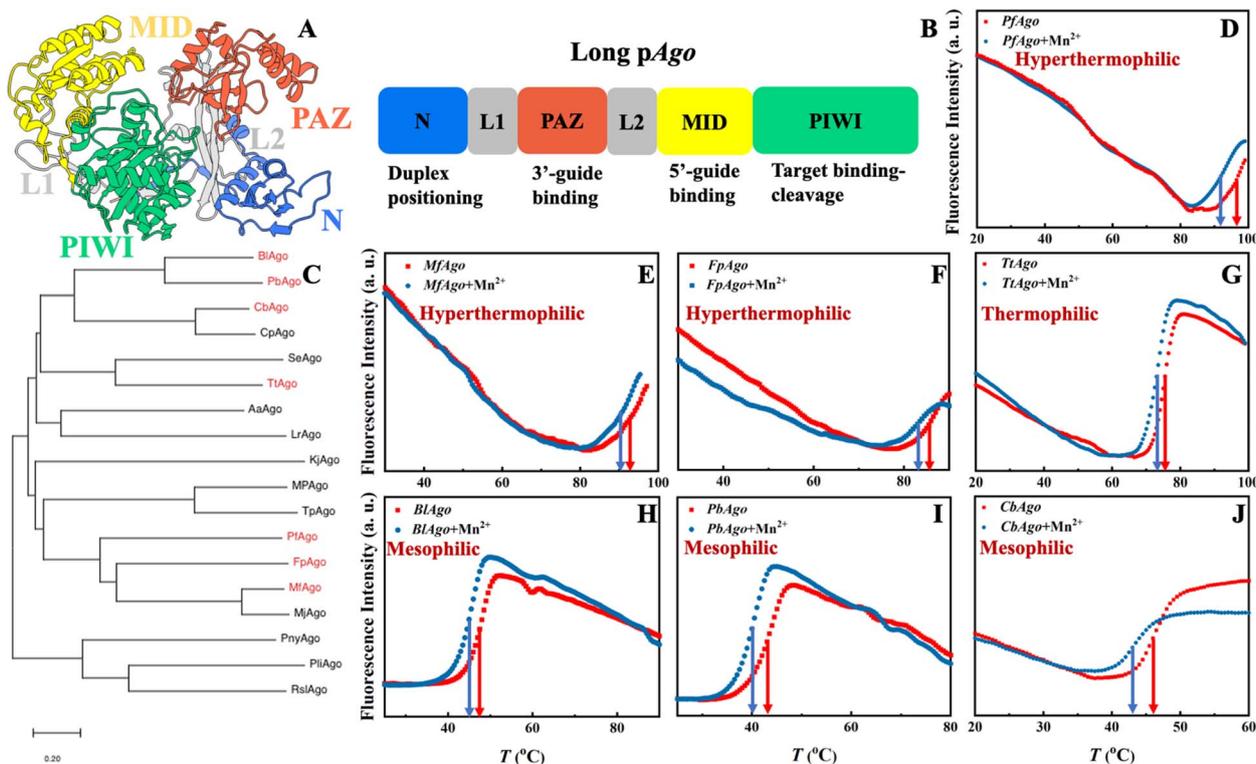
Fig. 1 Structural analysis of hyperthermophilic, thermophilic, and mesophilic pAgo proteins incubated with and without Mn^{2+} at different temperatures. (A) Representation of the domain architectures of long pAgo proteins. PAZ domain, MID domain, N domain, and PIWI domain are colored in red, yellow, blue, and green, respectively. (B) Schematic diagram of the domain organization of long pAgo proteins. (C) Maximum likelihood phylogenetic tree of characterized pAgo proteins. DSF spectra of (D) PfAgo, (E) MfAgo, (F) FpAgo, (G) TtAgo, (H) BlAgo, (I) PbAgo, and (J) CbAgo incubated with and without Mn^{2+} measured at different temperatures. The concentration of Mn^{2+} is 5 mM, which is widely applied in the biochemical assay of pAgo proteins. The solid arrows in panels D–J indicate the melting temperature, T_m.

a significant decrease in the T_m of pAgo proteins, reducing the thermostability, whereas other divalent cations (Mg^{2+}, Ca^{2+}, and Zn^{2+}) do not have this effect (Fig. S2D–E†). To further validate this finding, the T_m of pAgo proteins was also estimated by nano DSC, which measures the heat capacity of a protein as a function of temperatures.[41] The results obtained through nano DSC were consistent with those obtained through DSF spectroscopy, i.e., a similar trend of increased denaturation in the presence of Mn^{2+} (Fig. S3†). Interestingly, we found that there is no significant difference observed when the T_m of the secondary structure of pAgo proteins was evaluated under similar conditions (Fig. S4†). Thus, the above results suggest that the presence of Mn^{2+} could disrupt interactions between amino acids participating in the tertiary structure of the protein but not those involved in the secondary structure (alpha-helix and beta-sheet), thereby reducing the thermostability of the protein.

To gain a deeper understanding of the structural factors that contribute to the observed difference in T_m between pAgo proteins incubated with Mn^{2+} and those incubated without, we conducted all-atom molecular dynamics (MD) simulations on mesophilic (CbAgo), thermophilic (TtAgo), and hyperthermophilic (FpAgo) pAgo proteins incubated with and without Mn^{2+}. The example of snapshots of MD simulations is shown in Fig. S5† (the example of the potential energy of protein as a function of MD simulation time is shown in Fig. S6†). Our simulations reveal that the pAgo proteins incubated without Mn^{2+} exhibit a greater number of hydrogen bonds when compared to those incubated with Mn^{2+}, while the number of salt bridges remains constant (Table 1). This disparity in intermolecular interactions, i.e., loss of hydrogen bonds, could reduce the energy barrier for protein unfolding in pAgo proteins incubated with Mn^{2+}, which explains the decreased T_m observed in pAgo proteins (Fig. 1D–J).

By integrating the results of CD, DSF, and MD simulations, it suggests that Mn^{2+} possesses the capacity to perturb the intermolecular interactions among amino acid residues participating in the building of the tertiary structure, while not for the secondary structure (Table S1†).

Table 1 Number of hydrogen bonds and salt bridges of pAgo proteins incubated with and without Mn^{2+}

Protein	FpAgo	FpAgo + Mn^{2+}	TtAgo	TtAgo + Mn^{2+}	CbAgo	CbAgo + Mn^{2+}
Hydrogen bond[a]	611	588	452	438	307	282
Salt bridge[a]	13	13	11	11	9	9

[a] Number of hydrogen bonds and salt bridges are averaged over the entire simulation time.

It has been reported that structural flexibility is crucial for the biofunction of pAgo proteins.[22,24] The intriguing question then arises as to whether the decreased intermolecular interactions resulting from the addition of Mn^{2+} can increase the flexibility of pAgo proteins. To address this, we conducted a structural analysis of FpAgo, TtAgo, BlAgo, and CbAgo using synchrotron SAXS and Porod–Debye analysis.[24,42,43] The Porod–Debye analysis, which is a combination of the scattering intensity and the fourth power law of the scattering wavevector, $q^4 \cdot I(q)$, can be utilized to reveal the flexibility of biomacromolecules.[42] An unambiguous Porod plateau in the scattering profile indicates the protein takes a rigid structure, while a lack of a plateau implies that the biomacromolecule forms dynamic conformations.[42] As shown in Fig. 2A–D, the Porod–Debye plots of FpAgo, TtAgo, BlAgo, and CbAgo all displayed a clear Porod plateau. However, after incubation with Mn^{2+}, a significant change in the Porod–Debye region was observed, with a loss of the plateau suggesting the protein flexibility is

increased in the presence of Mn^{2+} (Fig. 2A–D). To further support these findings, we compared the flexibility of pAgo proteins incubated with and without Mn^{2+} using root mean square fluctuation (RMSF) derived from MD simulations. The RMSF of pAgo proteins incubated with Mn^{2+} is found to be larger than pAgo proteins incubated without Mn^{2+}, which indicates that Mn^{2+} confers increased flexibility to pAgo proteins (Fig. 2E–H). Our findings demonstrate that Mn^{2+} has a universal effect on enhancing the structural dynamics of pAgo proteins from different prokaryotes.

Furthermore, we compared the structural compactness of pAgo proteins incubated with and without Mn^{2+}. By utilizing Guinier analysis,[44,45] one can derive the radius of gyration (R_g) of the protein, and we found that R_g of pAgo proteins incubated with Mn^{2+} is comparable to that of pAgo proteins incubated without Mn^{2+} (Fig. 2I, S7–S17, and Table S3†), which is in agreement with the R_g derived from MD simulations (Fig. S18 and S19†). Furthermore, the Porod volume of pAgo proteins
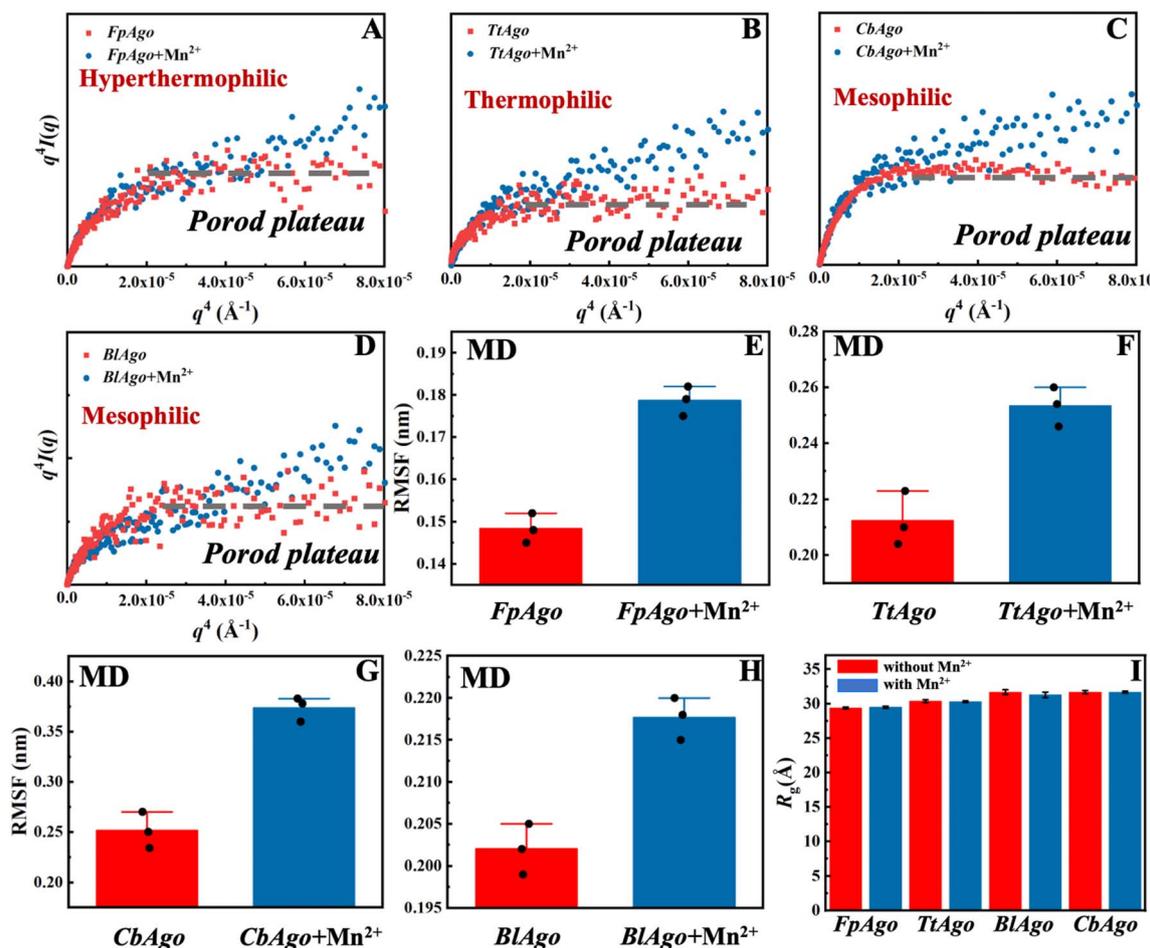

Fig. 2 Structures and dynamics of pAgo proteins incubated with and without Mn^{2+} derived from SAXS and MD simulation. Porod–Debye analysis, $q^4 I(q)$ vs. q^4, of (A) FpAgo, (B) TtAgo, (C) BlAgo, and (D) CbAgo incubated with and without Mn^{2+}. The concentration of Mn^{2+} is 5 mM. The dashed gray line in each panel indicates the Porod plateau. The details about the SAXS data collection and analysis are summarized in Materials and methods. Comparison of RMSF of (E) FpAgo, (F) TtAgo, (G) CbAgo, and (H) BlAgo incubated with and without Mn^{2+}. RMSF of pAgo proteins is averaged over entire residues. The results from three independent MD simulations were quantified. Error bars represent the standard deviations of three independent simulations. The detailed procedure is presented in the Materials and methods. (I) R_g of FpAgo, TtAgo, BlAgo, and CbAgo incubated with and without Mn^{2+} derived from SAXS. The Guinier plots of proteins are shown in Fig. S7–S17.†

incubated with and without Mn^{2+} was found to be similar, indicating that Mn^{2+} does not have a significant impact on the overall compactness of pAgo proteins. These findings were also supported by the *ab initio* low-resolution model reconstructed from SAXS data. As shown in Fig. S20,† the *ab initio* structure of pAgo proteins incubated with Mn^{2+} is similar to that of pAgo proteins incubated without Mn^{2+}.

The findings from DSF, CD, nano DSC, SAXS, and MD simulation studies provide a convincing explanation of Mn^{2+}'s impact on the structural flexibility of pAgo proteins, which demonstrates that the presence of Mn^{2+} greatly enhances the protein flexibility while preserving the protein's secondary structure. The observation that the overall structure of pAgo proteins remains similar to the crystalline form when incubated with Mn^{2+} further supports this conclusion, indicating that the flexibility changes are not due to significant alterations in the protein's overall structure.

Enzymatic functional role of the Mn^{2+}-induced flexibility in pAgo proteins

The physical characterization of Mn^{2+} has revealed that it can enhance the flexibility of pAgo proteins. However, the implications of this increase in flexibility on the catalytic function of pAgo proteins remain unclear. As shown in Fig. 3A, the catalytic cycle of pAgo proteins involves several functional steps, including binding guide (gDNA binding), target recognition and annealing (tDNA binding), target cleavage, and release (tDNA cleaving and releasing).[22,46] Firstly, we investigated the impact of increased protein structural flexibility on gDNA binding. We employed the fluorescence polarization assay on *Pli*Ago (DSF measurements of *Pli*Ago incubated with and without Mn^{2+} are shown in Fig. S21A†), a unique protein that does not require Mn^{2+} for substrate binding.[30] The result, as shown in Fig. 3B, indicates that as the concentration of Mn^{2+} increases, the dissociate constant K_d decreases, thus demonstrating an increased binding of gDNA to the protein and the formation of the more protein-gDNA binary complex. To further verify these results, we conducted gDNA binding experiments on *Cb*Ago using a mutation on the binding site amino acids, resulting in a binding pocket in the MID domain that does not bind Mn^{2+} (the amino acids sequence is shown in Table S5†).[30] We found that the *Cb*Ago mutant (*Cb*Ago*M*) incubated with Mn^{2+} has a greater binding affinity to gDNA than it incubated without Mn^{2+} (Fig. 3C). We also performed the electrophoretic mobility shift assay (EMSA) on *Cb*Ago*M* binding to gDNA. The result, illustrated in Fig. S22,† indicates that with an increase in the concentration of Mn^{2+}, the amount of free gDNA decreases,
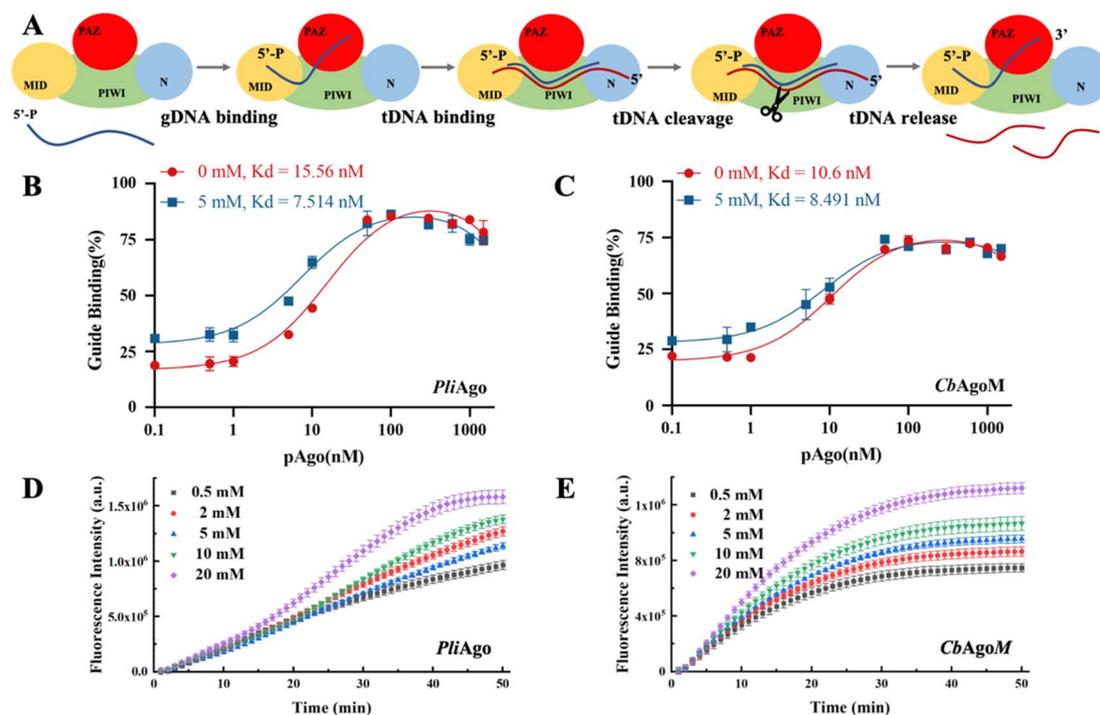

Fig. 3 The role of the Mn^{2+}-dependent structural dynamics of pAgo proteins for binding guide DNA and cleavage of target DNA. (A) Schematic diagram of DNA-catalytic cycle of pAgo proteins. Fluorescence polarization assay of the binding of (B) *Pli*Ago and (C) *Cb*Ago*M* to gDNA at different concentrations of Mn^{2+}. Cleavage assays of (D) *Pli*Ago and (E) *Cb*Ago*M* incubated with different concentrations of Mn^{2+}. The cleavage activity of pAgo proteins is traced by fluorescence intensity as a function of time. In all experiments, protein, guide, and target were mixed at a 5 : 1 : 1 molar ratio and incubated at 37 °C. The reaction buffer without Mn^{2+} contains 10 mM EDTA. Three samples were used for each experimental condition. The results from three independent experiments were quantified. Error bars represent the standard deviations of three independent experiments. The detailed procedure is presented in the Materials and methods. The nucleotide sequences of the gDNA and tDNA are presented in Table S4.†

while the protein–gDNA binary complex increases. This observation also demonstrates an enhanced binding of gDNA when the protein is incubated with Mn^{2+}. The above results provide additional support for the notion that the increase in protein flexibility caused by Mn^{2+} can enhance the binding ability of proteins to gDNA (DSF measurements of *CbAgoM* incubated with and without Mn^{2+} are shown in Fig. S21B†). Additionally, an increased quantity of protein–gDNA binary complexes can effectively function as templates, thereby facilitating the binding of a greater amount of tDNA.

The process of cleavage and release of tDNA is of paramount importance for the subsequent rounds of tDNA cleavage mediated by pAgo proteins.[22] To investigate the impact of Mn^{2+} on the cleavage efficiency of pAgo proteins on tDNA, we employed a highly sensitive fluorescence-based assay. To this end, we labeled the 5′- and 3′-end of tDNA with the fluorescent group 6′ FAM and quenching group BHQ1, respectively. This allowed us to monitor the cleavage and release process of pAgo proteins on tDNA in real-time, with the absence of a fluorescent signal indicating that tDNA was either not cleaved or had been cleaved but not yet released, and the presence of a fluorescent signal indicating that tDNA had been cleaved and released successfully. As depicted in Fig. 3D and E, the cleavage rate and yield of cleavage products of *PliAgo* and *CbAgoM* on tDNA exhibited a clear dependence on the concentration of Mn^{2+}, with tested higher concentrations resulting in increased cleavage products. Our findings provide important insights into the role of Mn^{2+} in modulating the catalytic activity of pAgo proteins, indicating that the enhancement of protein flexibility brought about by Mn^{2+} might facilitate conformational changes during the cleavage process and the release of products.

It has been reported that small interfering DNA of varying lengths present inside cells can function as gDNA for proteins, which subsequently cleave invading DNA.[47] In light of this, we explored the flexibility of pAgo proteins and their potential roles in facilitating binding to tDNA and gDNA of different lengths. Our analysis, illustrated in Fig. S23,† revealed that when the concentration of Mn^{2+} increases from 0.1 mM to 5 mM, K_d for the protein with tDNA and gDNA of various lengths decreases, indicating enhanced binding of gDNA and tDNA to the pAgo protein. These findings suggest that the ability of pAgo proteins to adapt their conformation, facilitated by an increase in structural flexibility induced by Mn^{2+}, enables them to bind to tDNA and gDNA of varying lengths.

We then investigated the effect of Mn^{2+}-induced flexibility in proteins on the cleavage and release of tDNA of varying lengths. Our experiments utilized a range of Mn^{2+} concentrations to measure the rate of tDNA cleavage and release. As shown in Fig. S24,† the results revealed a statistically significant positive correlation between increasing concentrations of Mn^{2+} and the fluorescence intensity per unit of time. This observation demonstrates an augmentation in the rate of tDNA cleavage and release in response to Mn^{2+}-induced changes in pAgo protein flexibility, thus suggesting that the enhancement of pAgo protein flexibility serves as a facilitative mechanism for the cleavage and release of tDNA.

Mn^{2+}-dependent precision cleavage of target DNA

It's widely recognized that the efficiency of pAgo's cleavage is influenced by mismatches that occur between the guide and the target, particularly within the seed region. The presence of these mismatches can cause "bubbles" to form between the guide and the target, consequently affecting their mutual recognition and the subsequent cleavage by pAgo (Fig. 4A). In this section, we also mutated the amino acids in the binding pocket of pAgo proteins to exclude the impact of Mn^{2+} on binding gDNA and tDNA.[30] In the case of *PfAgo*, the introduction of a single nucleotide mismatch at varying positions within the guide can cause weakening or even elimination of target cleavage (Fig. 4B). Interestingly, when the concentration of Mn^{2+} is increased, *PfAgo* can cleave the target even with a mismatched guide (Fig. 4B). This suggests that Mn^{2+} enhances the flexibility of *PfAgo*, thereby increasing its tolerance for mismatches. We then selected three guides that either perfectly matched the target sequence (guide-m0) or contained mismatches at the fourth (guide-m4) and seventh (guide-m7) positions. We performed cleavage assays at gradually increasing Mn^{2+} concentrations (Fig. 4C and D). Under conditions of 0.1 mM Mn^{2+}, the three guides directed varied catalytic efficiency, ranging from 20% to 70%. Conversely, when the Mn^{2+} concentration was increased to 1 mM, the cleavage efficiency of all three guides reached a comparable level. Similarly, *CbAgo* demonstrated enhanced activity with increasing Mn^{2+} concentrations, as shown in Fig. S25.†

To further investigate the role of Mn^{2+}, we conducted fluorescence polarization experiments to measure the apparent dissociation constants (K_d) of *PfAgo* with either the guide or the target at different Mn^{2+} concentrations. We observed that an increase in the concentration of Mn^{2+} enhances the affinity of *PfAgo* for both the guide and the target. For the guides, the K_d values increased up to 4-fold and 2-fold for guide-m0 and guide-m4, respectively. For the target, the K_d values increased 3-fold (Fig. 4E). These findings suggest an increased binding affinity of the protein for mismatched gDNA and tDNA, which is attributed to increased protein flexibility under elevated Mn^{2+} concentrations. This provides further support for our hypothesis that Mn^{2+} may play a crucial role in enhancing the tolerance of DNA cleavage to mismatches.

Thus, the data obtained indicate that the enhancement of flexibility in pAgo proteins, induced by Mn^{2+}, broadens the tolerance for mismatches between the gDNA and the tDNA. This heightened tolerance, however, incurs a trade-off, leading to a consequent decrease in the precision of tDNA cleavage orchestrated by the protein. This pivotal finding underscores the profound implications of the interplay between protein flexibility and nucleic acid detection accuracy, highlighting the necessity for maintaining an optimal balance between these two critical factors.

Mn^{2+}-dependent dynamical states in pAgo protein derived from MD simulations

To gain a more atomic-level understanding of the impact of Mn^{2+} on the conformational dynamics related to the
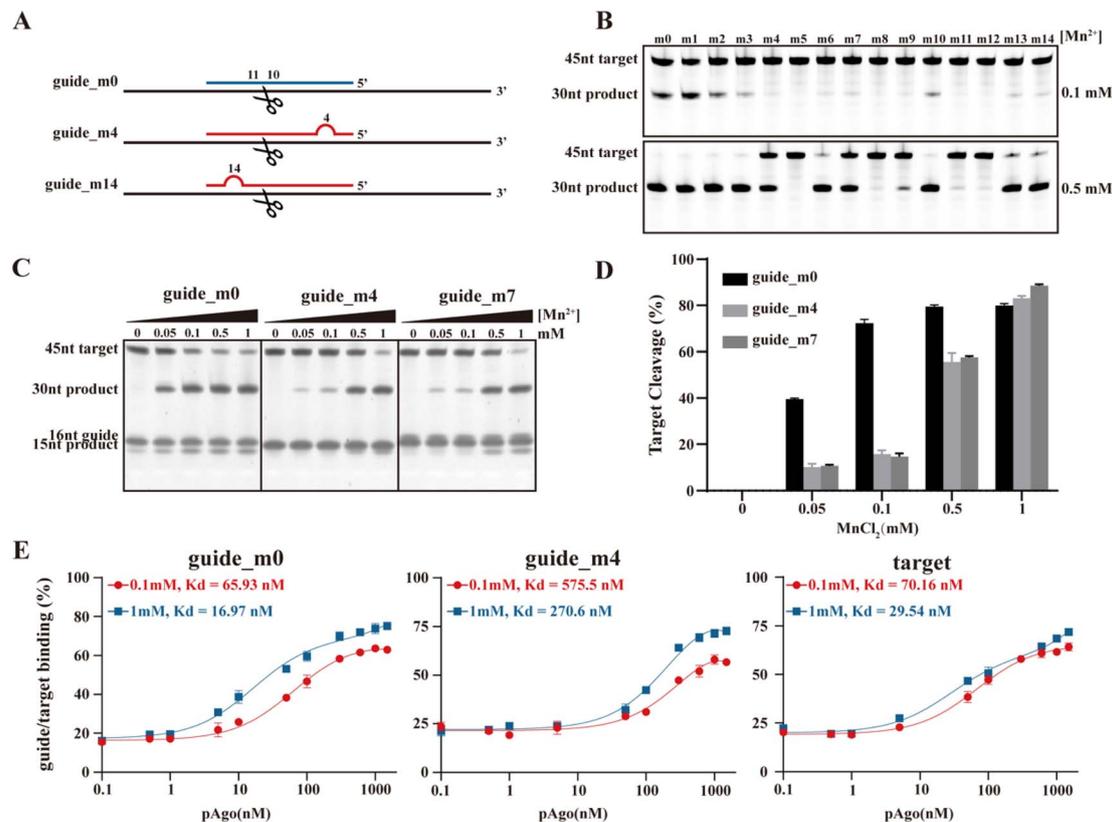
Fig. 4 The role of the Mn^{2+}-dependent structural dynamics of pAgo proteins for the designed mismatched guide DNA directed cleavage on target DNA. (A) Schematic representation of the designed mismatched gDNA directed cleavage on tDNA. The introduced mismatched nucleotides are indicated by the red semicircle. The nucleic acids sequence of gDNA and tDNA are shown in Table S6.† *Pf*Ago is used here. (B) and (C) Gel detection results for the designed mismatched gDNA-directed cleavage on tDNA at different concentrations of Mn^{2+}. (D) Quantifying the effects of incubating with Mn^{2+} on tDNA cleavage obtained from panel (C). (E) Fluorescence polarization assay of the designed mismatched guide and target at different concentrations of Mn^{2+}. The results from three independent experiments were quantified. Error bars represent the standard deviations of three independent experiments. It should be noted that we mutated the amino acids in the binding pocket of pAgo proteins to exclude the impact of Mn^{2+} on binding gDNA and tDNA.

functionality of pAgo proteins, we conducted MD simulations of pAgo protein both incubated with and without Mn^{2+} mimicking the experimental conditions. As can be seen in Fig. S27,† the SAXS profile calculated from MD simulation agrees quantitatively with the experimental profile, demonstrating that the *Cb*Ago obtained experimentally after incubation with Mn^{2+} can be described by the MD-derived structures.

Firstly, we analyzed the overall conformational changes in proteins in the presence of Mn^{2+}. Fig. 5A compares the conformation of *Cb*Ago incubated without Mn^{2+} (upper panel) to that of *Cb*Ago with Mn^{2+} (lower panel) over the trajectory time. The result shows that the addition of Mn^{2+} leads to an increase in the conformational dynamics of *Cb*Ago. This finding is further validated by the observation that the root mean square fluctuation (RMSF) of proteins increases in the presence of Mn^{2+} (Fig. 5B). Although the flexibility of the protein is enhanced by Mn^{2+}, the secondary structure and the radius of gyration remain consistent regardless of the presence of Mn^{2+}, aligning with the SAXS and CD results presented in Fig. 1 and 2. Additionally, when analyzing the conformational phase space of

*Cb*Ago sampled in the MD simulation, we observed that the presence of Mn^{2+} allows the protein to explore a significantly larger conformational space (Fig. 5C and D). We also analyzed the locations of Mn^{2+} on protein at the molecular level. As shown in Fig. S24,† Mn^{2+} on the surfaces of different protein domains (N, Linker 1, PAZ, Linker 2, MID, and PIWI) engages in electrostatic interactions with amino acids. These interactions disrupt hydrogen bonds in the protein surface (Table 1), which leads to an enhancement in the structural flexibility of the protein. This finding aligns with the increased RMSF of the protein after incubating with Mn^{2+} (Fig. 5B). Specifically, Mn^{2+} plays a crucial role in interacting with Linker 1 and Linker 2 (Fig. S24†), contributing to the motion of the PAZ domain, which is known to be essential for the functionality of pAgo proteins.[22]

Secondly, we analyzed the conformational changes related to the specific functionality of proteins.

Guide nucleic acid binding. pAgo protein should first bind to guide nucleic acids (Fig. 6A). The conformational mobility of the PAZ domain, observed upon incubation with Mn^{2+}, is
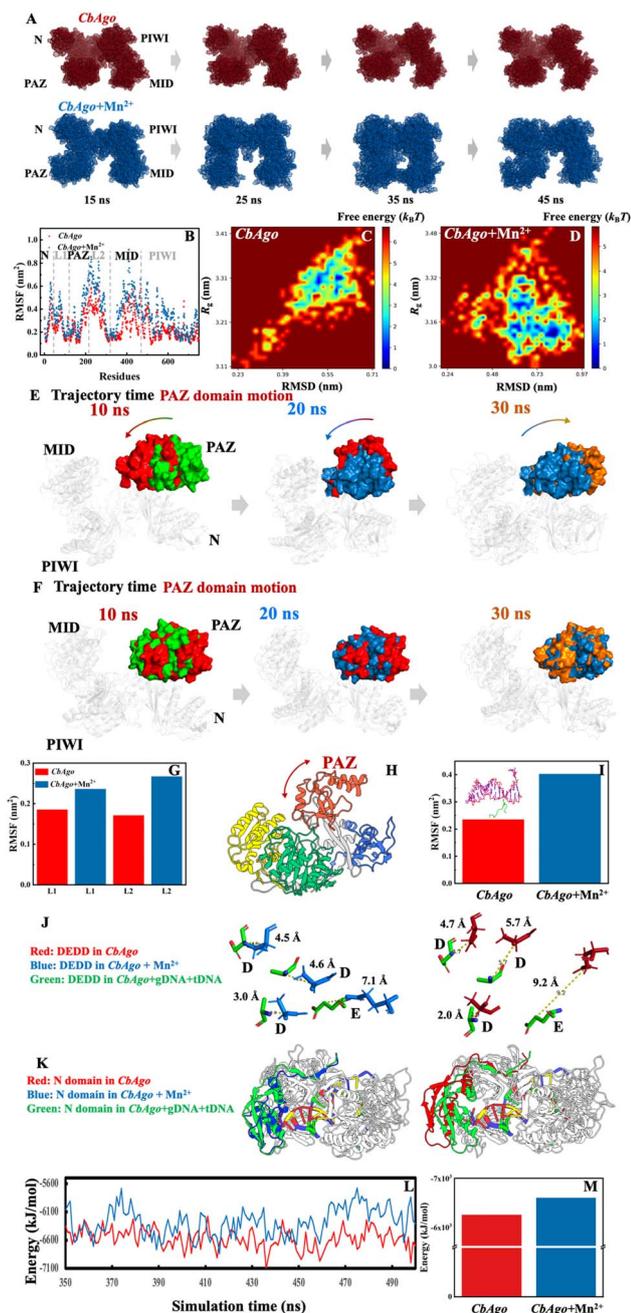
Fig. 5 The effect of Mn^{2+} on the structural dynamics of pAgo protein derived from MD simulations. (A) The MD-derived structure of CbAgo incubated with (blue) and without (red) the presence of Mn^{2+} at different simulation times. (B) Comparison of RMSF of the overall structure. Free energy landscape of CbAgo incubated (C) without and (D) with Mn^{2+}. RMSD is the root mean squared deviation of the structure in the first MD snapshot after equilibration. Conformational change of PAZ domain in CbAgo incubated (E) with and (F) without Mn^{2+} obtained from MD simulation. Comparison of RMSF of (G) linkers and (I) catalytic loop of CbAgo incubated with and without Mn^{2+}. (H) Scheme of the motion of PAZ domain in pAgo protein. (J) Structural alignment of catalytic sites of CbAgo incubated without (left panel) and with (right panel) Mn^{2+} with respect to that of the experimental functional conformation (PDB ID: 6qzk). Catalytic sites, DEDD, in CbAgo incubated without Mn^{2+}, with Mn^{2+}, and in the experimental functional form are highlighted in red, blue, and green, respectively. (K) Structural alignment of N domain of CbAgo incubated without (left panel) and with (right panel) Mn^{2+} with respect to

significantly greater than that of protein incubated without Mn^{2+} over the trajectory time (Fig. 5E and F). This phenomenon can be attributed to the increased flexibility present in the Linker 1 and Linker 2 regions between the N domain and the MID domain, respectively (Fig. 5G and H). The enhanced conformational mobility of the PAZ domain could facilitate the capability of various pAgo proteins to engage with diverse populations of ssDNAs of varying lengths.[21,22,25]

Propagation of duplexes and cleavage of target. After binding to guide nucleic acids, the protein–guide binary complex then binds to and cleaves target nucleic acids (Fig. 6B). The binding of the target nucleic acids leads to structural modifications of pAgo proteins, including rotations of the PAZ domain and alterations in the conformations of loops within the PIWI domain.[22,27,34,48] These changes propagate the nucleic acid duplex within the catalytic cleft of the pAgo protein and activate catalysis.

Specifically, the glutamic loop, as shown in Fig. 5I, can adopt distinct conformations in the presence of the target strand. It inserts into the catalytic sites and binds metal ions during the formation of the extended guide–target duplex. Therefore, the enhanced conformational dynamics in the PAZ domain (Fig. 5G) and catalytic loop (Fig. 5I) promote the closure of the binding cleft and activate the cleavage of the target (Fig. 6C).[21,23]

Furthermore, we also observed that the catalytic tetrads adjust their alignments to functional ones, thereby reducing the energy barrier for conformational change (Fig. 5J), which accelerates the cleavage of target nucleic acid (Fig. 6D).

Target release and preparation for the next round of catalysis. After the cleavage of target nucleic acids, proteins will release the cleaved nucleic acids for the next round of catalysis (Fig. 6E). As shown in Fig. 5K, Mn^{2+} induces the adjustment of the N domain position closer to its functional conformation, which contributes to the promotion of unwinding between the guide and target after cleavage.[28,29] Additionally, the increased flexibility in the glutamic loop and linkers could facilitate the unplugging of the active sites and the restoration of the PAZ domain, respectively. This process then regenerates the binary guide-pAgo complex for the next round of catalysis (Fig. 6F).

Furthermore, we analyzed the binding energy[49] of protein to DNA in both the presence and absence of Mn^{2+}. The results show that the binding energy of the protein to DNA is reduced upon the addition of Mn^{2+} throughout the simulation time (Fig. 5L and M). This finding also validates that the presence of Mn^{2+} can facilitate the release of cleaved target nucleic acids and promote the re-adjustment of conformations.

that of the experimental functional conformation (PDB ID: 6QZK). N domain in CbAgo incubated without Mn^{2+}, with Mn^{2+}, and in the experimental functional form is highlighted in red, blue, and green, respectively. Here, the protein structure is aligned by PyMOL. The alignment on C_{alpha} is achieved by using PyMOL software. (L) The binding energy of CbAgo to gDNA/tDNA duplex over the entire simulation time derived from MD simulations. (M) The averaged binding energy of CbAgo to gDNA/tDNA duplex. The initial structure of MD simulation is the protein–gDNA–tDNA tertiary complex (PDB ID: 6QZK).
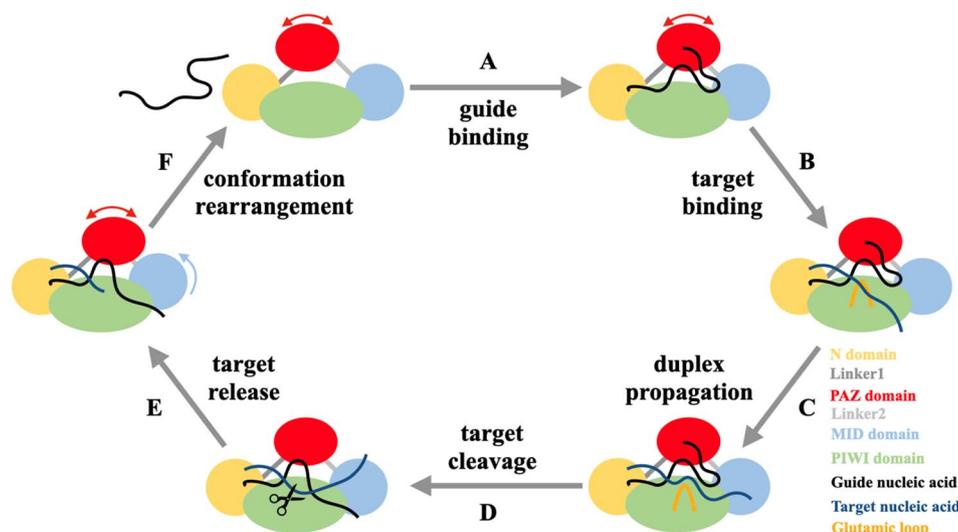
Fig. 6 The catalytic cycle of pAgo proteins. Guide-loaded pAgo protein performs a search for a complementary target through base-pairing with the seed region of the guide strand, followed by duplex propagation. Conformational mobility of the PAZ domain facilitates correct base-pairing. Conformational changes in the active site allow the binding of metal ions, followed by cleavage of the target strand and its stepwise release from the complex.

Discussion

Divalent cations play a fundamental role in biomacromolecule dynamics, primarily situated in ribosomes,[50,51] enzymes,[30,52,53] and structural proteins.[54] The proper function and stability of such proteins necessitate the presence of ions. Divalent ions can impart consequential effects on the conformation and functionality of proteins, which is integral to numerous biological processes like enzymatic catalysis,[31] regulation of protein–protein interactions,[54] and signal transduction.[55] Divalent ions also play a pivotal role in the regulation of membrane transport phenomena like ion transit across the plasma membrane and intracellular movement of ions and molecules.[56] In ion channels and pumps, divalent ions serve as indispensable regulators, controlling the opening and closing of these channels, thereby regulating the flux of ions into and out of cells.[56] Additionally, it has been demonstrated that ions impact the activity of endonucleases. For instance, the Mg^{2+}-dependent conformational rearrangements of the CRISPR-Cas12a R-loop complex are crucial for complete double-stranded DNA cleavage.[52]

In the case of pAgo proteins, we unraveled the molecular mechanisms of unbound Mn^{2+} regulating the binding, cleavage, and release of products through the use of spectroscopy, biochemical assays, and MD simulation. Initially, the presence of Mn^{2+} can disrupt certain hydrogen bonds within non-secondary structures, thereby increasing the flexibility of proteins and the associated entropy, without compromising the structural integrity. Next owing to the increased flexibility of the L1 linker and L2 linker, the conformational number of the PAZ domain is significantly increased. This enhanced structural flexibility facilitates the binding of the pAgo protein to gDNA, and helps the PAZ domain recognize gDNA of varying lengths. Furthermore, the enhanced structural variability of the

glutamic loop and PAZ domain aids in the propagation of the DNA duplex, preparing it for tDNA cleavage. In addition, once the holo-form arrangement is achieved by the catalytic sites and the N domain, the catalytic center in the PIWI domain can be exposed to the tDNA. This exposure allows for the cleavage of the tDNA, facilitating the release of the cleaved product. Our simulation data indicates that the energy barrier for releasing the target in this step is also lowered by the presence of Mn^{2+}. The analysis of the conformational dynamics of this catalytic cycle reveals that the presence of Mn^{2+} reduces the energy barrier for conformational changes between different functional conformations. Furthermore, this result unveiled the unexpected dynamical role of unbound Mn^{2+} in increasing the conformation states of pAgo proteins, which is crucial for their catalytic functions.

Previous structural research, based on crystallography, has demonstrated that pAgo proteins must undergo significant conformational changes to implement their functions, including the rearrangement of catalytic tetrads, propagation of duplexes through shifting loops in the PIWI domain, and motion of the PAZ domain, and release of cleaved targets by adjusting the PAZ and N domains.[21] Therefore, structural flexibility is crucial for the conformational arrangement needed to achieve the functionality of pAgo proteins at different stages. In our study, we found that pAgo proteins from mesophiles, thermophiles, and hyperthermophiles exhibit a significant increase in flexibility when unbounded Mn^{2+} is present.

We found that Mn^{2+} can induce the structural flexibility of pAgo proteins from various prokaryotes, thereby promoting the rapid binding of the protein to gDNA and the formation of a stable protein-guide binary complex. This complex serves as a template to recognize various target nucleic acids in a short period. Furthermore, we observed that an increase in Mn^{2+} concentration can enhance the tolerance of cleavage to

mismatches between guide DNA and target DNA. In prokaryotes, it has been demonstrated that pAgo proteins widely participate in hosts to defend against the invasion of nucleic acids[2,47] According to our results, we can speculate that the increase in protein structural flexibility induced by Mn^{2+} can assist microorganisms in efficiently resisting external viral invasions. Firstly, the Mn^{2+}-enhanced flexibility of protein structure can aid pAgo proteins in binding to plasmids, quickly chopping the plasmids to generate guide nucleic acids for recognition of invading nucleic acids. Next, the increased structural flexibility of pAgo proteins facilitates rapid conformational modifications. This allows them to quickly bind with different types (sequences and lengths) of nucleic acids in hosts and identify various invading nucleic acids, such as phages. Finally, the increased flexibility in pAgo proteins can aid in the protein's cleavage of mismatched nucleic acids, suggesting that the pAgo proteins in the cell may utilize a sequence of guide nucleic acids to bind to target nucleic acids with different sequences or lengths more efficiently. This, in turn, enhances the recognition and cleavage of invading DNA, preventing the replication of invader nucleic acids and ultimately safeguarding the host.

pAgo proteins have been widely used in nucleic acid detection.[6,7,12] pAgo protein can bind to different gDNAs, which allows it to specifically recognize various complementary tDNAs. This capability enables the simultaneous detection of various diseases in argonaute-mediated nucleic acid diagnostics.[7] In this study, we found that Mn^{2+}-induced structural flexibility in the protein significantly enhances the binding affinity of pAgo protein to gDNAs of different lengths and sequences, without exhibiting a preference for a specific gDNA. This expanded improvement in the gDNA binding affinity profile of pAgo proteins suggests that elevating the concentration of Mn^{2+} in the detection system can trigger rapid binding of pAgo proteins to diverse gDNAs. This results in the formation of stable protein–gDNA binary complexes, facilitating the swift identification of various tDNAs and thereby accomplishing the goal of fast nucleic acid detection. Moreover, the current regulation of protein binding affinity is primarily accomplished through the mutation of amino acids in the protein—a method that is both time-consuming and costly.[57,58] Nevertheless, our results indicate that it is possible to adjust the binding affinity of pAgo to gDNA by regulating ion concentrations, whether increasing or decreasing them, to meet specific requirements in nucleic acid detection. This approach could offer a simpler and more cost-effective alternative for argonaute-based nucleic acid detection.

The precision of nucleic acid detection methodologies is critically reliant on the accurate cleavage by pAgos. The high fidelity of such assays is underpinned by the exactness of the initial DNA cleavage process. Any deviations or inaccuracies within this fundamental step can substantially diminish the efficiency of subsequent amplification and signal readout stages.[6] Our findings shed light on the role of Mn^{2+}-induced flexibility in augmenting the proficiency of the pAgo protein in handling mismatches between gDNA and tDNA. We observed a correlation between increased concentrations of Mn^{2+} and an enhanced capacity of the pAgo protein to accommodate gDNA and tDNA mismatches, facilitating tDNA cleavage. The elevated presence of Mn^{2+} could enhance the protein's conformational flexibility and various functional states, which is verified by the MD simulations. This increased structural flexibility enables the protein to adapt its conformational state to cater to a variety of mismatch scenarios, thus improving the efficiency of tDNA cleavage. These findings carry significant implications for the effectiveness of various recently developed nucleic acid detection technologies.[5,6]

Conclusion

In this study, we investigated how the unbound Mn^{2+} affects the dynamics, structure, and endonuclease activity of pAgo proteins obtained from mesophilic (CbAgo, BlAgo, PliAgo, and PbAgo), thermophilic (TtAgo), and hyperthermophilic (PfAgo, FpAgo, and MfAgo) microorganisms using a combination of experimental and computational methods. Our results indicated that the presence of these unbound Mn^{2+} reduces the hydrogen bonds in pAgo proteins to release a great degree of structural flexibility while maintaining the overall structural integrity. Biochemical assays revealed that this Mn^{2+}-induced structural flexibility in pAgo proteins significantly increases the substrate affinity and facilitates the binding of guide and target strands. Complementary computer simulations confirmed these experimental findings and revealed that the increased flexibility of Linker 1 and Linker 2 promotes the conformational mobility of the PAZ domain, allowing for the recognition of guide and target strands of varying lengths. Additionally, changes in the conformations of the PAZ domain and glutamic finger promote the propagation of the duplex. By comparing the structures of pAgo proteins incubated with Mn^{2+} to those of the protein–guide–target ternary complex, we observed that the conformation of catalytic sites and N domain shifts towards a functional state, which reduces the energy cost of conformational changes required for the cleavage of target strand and the release of the products.

Our findings reveal that unbound Mn^{2+} plays an important role in the endonuclease functions of pAgo proteins, and this mechanism is a general strategy employed by pAgo proteins to enhance their catalytic functions. Unlike previous structural studies, which highlight the importance of the bound Mn^{2+} in directly participating in guide binding and target cleavage, our work discovers a role of unbound Mn^{2+} in an indirect way. The unbound free Mn^{2+} plays a crucial part in promoting the structural flexibility of pAgo proteins. This benefit extends not only to the binding of the protein to guide and target DNA, but also to the cleavage and release processes.

More importantly, by harnessing the influence of protein flexibility induced by unbound Mn^{2+} on the degree of mismatch between guide and target nucleic acids, we can finely tune the precision of target recognition by pAgo proteins through the modulation of Mn^{2+} concentration. This crucial characteristic expands the scope of molecular diagnostic applications, further highlighting the significance of structural flexibility in optimizing the performance of pAgo proteins.

Materials and methods

Protein expression and purification

A codon-optimized version of the *Pf*Ago, *Tt*Ago, *Fp*Ago, *Mf*Ago, *Bl*Ago, *Pb*Ago, *Cb*Ago, *Cb*AgoM, and *Pli*Ago gene was synthesized by Sangon Biotech (Shanghai, China), and was cloned into the pET28a plasmid to construct pEX-Ago with an N terminal His-tag. The expression plasmid was transformed into *Escherichia coli* BL21 (DE3) cells. A 10 ml seed culture was grown at 37 °C in LB medium with 50 μg ml^{-1} kanamycin and was subsequently transferred to 1 L of LB in a shaker flask containing 50 μg ml^{-1} kanamycin. The cultures were incubated at 37 °C until the OD_{600} reached 0.6–0.8, and protein expression was then induced by the addition of isopropyl-D-thiogalactopyranoside (IPTG) to a final concentration of 0.5 mM, followed by incubation for 20–24 h at 18 °C. Cells were harvested by centrifugation for 30 min at 6000 rpm, and the cell pellets were collected for later purification. The cell pellets were resuspended in lysis buffer (15 mM Tris–HCl, 500 mM NaCl, pH 7.4) and then disrupted using a High-Pressure Homogenizer at 700–800 bar for 5 min (Gefran, Italy). The lysates were centrifuged for 30 min at 12 000 rpm at 4 °C, after which the supernatants were subjected to Ni-NTA affinity purification with elution buffer (15 mM Tris–HCl, 500 mM NaCl, 250 mM imidazole, pH 7.4). Further gel filtration purification using a Superdex 200 (GE Tech, USA) was carried out with an elution buffer. The fractions resulting from gel filtration were analyzed by SDS-PAGE, and fractions containing the protein were flash frozen at −80 °C in buffer (15 mM Tris–HCl pH 7.4, 200 mM NaCl, 10% glycerin).

Differential scanning fluorimetry

Each pAgo protein sample containing 1 μM of protein in a buffer containing 15 mM Tris–HCl (pH = 7.4) and 200 mM NaCl was prepared in triplicate and added to PCR tubes. To examine the effect of Mn^{2+} on pAgo proteins, pAgo proteins were incubated in Tris–HCl buffer (pH = 7.4) with 5 mM Mn^{2+} or 5 mM EDTA for 20 min. SYPRO Orange dye available as 5000× stock (Sigma-Aldrich) was added just before the measurement of the pAgo proteins in an appropriate amount to achieve a final concentration of the dye of 5×. The thermal denaturation of the pAgo proteins was monitored by exciting the SYPRO Orange dye at 470 nm and monitoring its fluorescence emission at 570 nm using Q-PCR (Analytikjena, Germany). The baseline correction is used by the Opticon Monitor software available on the PCR instrument.

Nano differential scanning calorimetry

Nano differential scanning calorimetry (nanoDSC) measurements were performed by using Nano DSC instruments (TA, USA). The concentration of pAgo proteins was 0.1 mg ml^{-1} in a buffer containing 15 mM Tris–HCl (pH 7.4) and 200 mM NaCl. To examine the effect of Mn^{2+} on pAgo proteins, pAgo proteins were incubated in 15 mM Tris–HCl buffer (pH = 7.4) with 5 mM Mn^{2+} or 5 mM EDTA for 20 min. All the experiments were carried out at temperatures ranging from 10 to 110 °C with a heating rate of 1 °C min^{-1} and under a pressure of 3 atm. The

melting curves of pAgo proteins were subtracted from the buffer scans.

Circular dichroism spectroscopy

The CD measurements on the evolution of the secondary structure of pAgo proteins were performed in a Jasco J-1500 spectropolarimeter with a 1 mm pathlength cell. The signals in the far-UV CD region (222 nm) were monitored as a function of temperature to determine the thermal unfolding of pAgo proteins. The concentrations of pAgo proteins were 0.1 mg ml^{-1} in 1× PBS buffer (pH = 7.4) for the various measurements. The pAgo proteins were heated in the range of 15 °C to 100 °C with a 1 °C min^{-1} heating rate and equilibrated for 3 min at each temperature, and the CD data were collected at 0.5 °C intervals. For CD spectra, we used PBS buffer as the solvent instead of Tris–HCl buffer because the Tris–HCl buffer has a strong CD background, which will significantly affect the analysis of the CD signal of proteins.[24]

Small-angle X-ray scattering

Small-angle X-ray scattering (SAXS) measurement was employed to monitor the structural evolution of pAgo proteins incubated with and without Mn^{2+}. *In situ* synchrotron SAXS measurements were conducted at BL19U2 beamline in Shanghai Synchrotron Radiation Facility (SSRF). The X-ray wavelength was 0.103 nm. Protein samples were dissolved in a buffer containing 15 mM Tris–HCl (pH 7.4), 200 mM NaCl, and 5 mM $MnCl_2$ or EDTA. The concentration of samples is 0.5 mg ml^{-1}. Protein solutions were loaded into the silica cell and then gently refreshed with a syringe pump to prevent X-ray damage. The measurements were carried out at 25 °C. To calculate the absolute intensity of protein, the empty cell and buffer were also measured at corresponding temperatures. Two-dimensional (2D) diffraction patterns were collected by the Pilatus 2 M detector with a resolution of 1043 × 981 pixels of 172 μm × 172 μm. Twenty sequential 2D images were collected with 0.5 s exposure time per frame. The 2D scattering patterns were then integrated into one-dimensional (1D) intensity curves by using Fit2D software from the European Synchrotron Radiation Facility (ESRF). Frames with no radiation damage were used for further processing. The SAXS data were compared to the atomic model by using the CRYSOL software.[59] *ab initio* reconstruction of protein structure by a chain-like ensemble of dummy residues is generated by GASBOR.[60] P1 (no symmetry) and monodisperse data mode were used in generating the GASBOR model. At least 10 iterations of GASBOR programs were independently performed to validate the models. A presentative of the most typical model obtained was used in the figures. The one-dimensional data is processed by using ScÅtter and ATSAS software.[61] The details of SAXS data collection and analysis are summarized in Table S3.†

Molecular dynamics simulations

In MD simulations, a standard simulation box typically contains approximately ∼55 000 molecules, encompassing water molecules, proteins, and Mn^{2+} in our study. Thus, there

are two ways to establish the simulation system for atomic-level analysis of protein dynamics. One approach (System 1, with a ratio of 1 protein: 6 Mn^{2+}: 55 000 water in a simulation box) involves the ratio between Mn^{2+} and water to mimic biophysical experiments, while the other approach (System 2, with a ratio of 1 protein: 5000 Mn^{2+}: 50 000 water in a simulation box) considers the ratio between Mn^{2+} and protein to mimic biophysical experiments. To determine which simulation system better agrees with the experimental system, we compared the SAXS profiles calculated from the MD protein structure with the SAXS profile calculated from experiments by using CRYSOL.[62] As shown in Fig. S27,† we observed that the Chi^2 values of the SAXS profile obtained from System 1 ($Chi^2 = 1.506$) are much closer to the experimental SAXS profile compared to the one calculated from System 2 ($Chi^2 = 30.964$). This result indicates that the MD structure from System 1 better aligns with the experimental structure. Therefore, we selected System 1 for further atomic-level analysis of pAgo protein dynamics.

The initial structures of *Cb*Ago and *Tt*Ago for simulations were taken from PDB crystal structures 6QZK and 4N47, respectively. The initial structures of *Bl*Ago and *Fp*Ago for simulations were taken from AlphaFold2.[63] The initial structure of *Cb*Ago–gDNA–tDNA for simulations was taken from PDB crystal structures 6QZK. Protein and a large number of water molecules were filled in a cubic box (see Fig. S5†). For proteins and complexes incubated with the Mn^{2+} system, 6 Mn^{2+} were added into the simulation box to mimic the experimental concentration, and 32 chlorine counter ions were added to keep the system neutral in charge. For proteins and complexes in an aqueous solution, 16 chlorine counter ions were added to keep the system neutral in charge. The CHARMM36m force field[64] was used for proteins, complex, and Mn^{2+}, and the CHARMM-modified TIP3P model was chosen for water. The simulations were carried out at 298 K. After the 4000-step energy-minimization procedure, the systems were heated and equilibrated for 100 ps in the NVT ensemble and 500 ps in the NPT ensemble. The 100 ns production simulations were carried out at 1 atm with the proper periodic boundary condition, and the integration step was set to 2 fs. Fig. S6† shows the 100 ns profile of potential energy as a function of MD trajectory time for *Cb*Ago incubated with and without Mn^{2+}. It was clear that the equilibration procedure was sufficient for minimizing the energy of protein structures. The covalent bonds with hydrogen atoms were constrained by the LINCS algorithm.[65] Lennard-Jones interactions were truncated at 12 Å with a force-switching function from 10 to 12 Å. The electrostatic interactions were calculated using the particle mesh Ewald method[66] with a cutoff of 12 Å on an approximately 1 Å grid with a fourth-order spline. The temperature and pressure of the system are controlled by the velocity rescaling thermostat[67] and the Parrinello–Rahman algorithm,[68] respectively. All MD simulations were performed using GROMACS 2020.4 software packages. Representative simulation snapshots of the systems are given in Fig. S5.†

Single-strand DNA cleavage assay

For standard activity assays, cleavage experiments were performed in a 5 : 1 : 1 molar ratio (protein : guide : target). First, 5 μM pAgo protein was mixed with a synthetic 1 μM gDNA guide in the reaction buffer (15 mM Tris–HCl (pH 7.4), 200 mM NaCl, different concentrations of $MnCl_2$ or 5 mM EDTA). The solution was then pre-incubated at 37 °C for 20 min. After pre-incubation, 1 μM tDNA, which was labeled with the fluorescent group 6-FAM at the 5′-end and the quencher BHQ1 at the 3′-end, was added to the mixture. The cleavage experiments were performed at 37 °C. All experiments were performed in triplicate, and the fluorescence signals were traced by the quantitative real-time PCR QuantStudio 5 (Thermo Fisher Scientific, USA) with $\lambda_{ex} = 495$ nm and $\lambda_{em} = 520$ nm. The results were analyzed by QuantStudioTM Design & Analysis Software v1.5.1. All the gDNA and tDNA used for cleavage are listed in Table S4.†

In this work, 5 mM Mn^{2+} is used in the majority of our study. 5 mM Mn^{2+} is widely used in the mechanistic studies of pAgo proteins and pAgo-mediate nucleic acid diagnostics.[7,69–74] Therefore, to ensure the practical relevance of our experimental results, we set the Mn^{2+} concentration to 5 mM in the majority of our experiments.

Fluorescence polarization assay

To determine the apparent dissociation constant (K_d) for proteins binding to either gDNA or tDNA, a fluorescence polarization assay was conducted using a multifunctional enzyme-linked immunosorbent assay plate reader (Spark, Tecan). A solution was prepared by combining 5 nM of 3′ 6-FAM labeled guide or target DNA with proteins across a concentration range of 0 to 1500 nM in a reaction buffer (15 mM Tris–HCl at pH 7.4, 200 mM NaCl, and 5 mM $MnCl_2$). This mixture was incubated at 37 °C for 1 hour and subsequently transferred to a light-protected 96-well ELISA plate. The degree of polarization was measured using the Spark Tecan plate reader, employing an excitation wavelength of 485 nm and an emission wavelength of 525 nm. All experiments were independently conducted three times. The binding percentages were analyzed using Microsoft Excel and Prism 8 (GraphPad) software. The data was fitted with the Hill equation, incorporating a Hill coefficient of 2 to 2.5.

Electrophoretic mobility shift assay

To examine the loading of gDNA onto pAgo proteins, proteins and 3′ end FAM-labeled guide were incubated in 20 μL of reaction buffer containing 15 mM Tris–HCl pH 7.4, 200 mM NaCl for 20 min at 37 °C. The concentration of 3′ end FAM labeled guide and protein was fixed as 1 μM and 5 μM, respectively, whereas the concentration of $MnCl_2$ varied. Then the samples were mixed with 5 μL 5× loading buffer (Tris–HCl (pH 7.4), 25% glycerin, Bromophenol blue) and resolved by 12% native PAGE. Nucleic acids were visualized using Gel Doc™ XR+.

Data availability

All the data are presented in ESI.†

Author contributions

Conflicts of interest

The authors declare no competing financial interests.

Acknowledgements

References

1 B. Koopal, *et al.*, Short prokaryotic Argonaute systems trigger cell death upon detection of invading DNA, *Cell*, 2022, **185**, 1471–1486.e1419.

2 D. C. Swarts, *et al.*, DNA-guided DNA interference by a prokaryotic Argonaute, *Nature*, 2014, **507**, 258–261.

3 D. C. Swarts, *et al.*, The evolutionary journey of Argonaute proteins, *Nat. Struct. Mol. Biol.*, 2014, **21**, 743–753.

4 J. W. Hegge, D. C. Swarts and J. van der Oost, Prokaryotic Argonaute proteins: novel genome-editing tools?, *Nat. Rev. Microbiol.*, 2018, **16**, 5–11.

5 J. Song, *et al.*, Highly specific enrichment of rare nucleic acid fractions using Thermus thermophilus argonaute with applications in cancer diagnostics, *Nucleic Acids Res.*, 2019, **48**, e19.

6 Q. Liu, *et al.*, Argonaute integrated single-tube PCR system enables supersensitive detection of rare mutations, *Nucleic Acids Res.*, 2021, **49**, e75.

7 R. He, *et al.*, Pyrococcus furiosus Argonaute-mediated nucleic acid detection, *Chem. Commun.*, 2019, **55**, 13219–13222.

8 Y. Qin, Y. Li and Y. Hu, Emerging Argonaute-based nucleic acid biosensors, *Trends Biotechnol.*, 2022, **40**, 910–914.

9 X. Li, *et al.*, Mesophilic Argonaute-based isothermal detection of SARS-CoV-2, *Front. Microbiol.*, 2022, **13**.

10 R. Vaiskunaite, J. Vainauskas, J. J. L. Morris, V. Potapov and J. Bitinaite, Programmable cleavage of linear double-stranded DNA by combined action of Argonaute CbAgo from Clostridium butyricum and nuclease deficient RecBC helicase from E. coli, *Nucleic Acids Res.*, 2022, **50**, 4616–4629.

11 G. Xun, S. T. Lane, V. A. Petrov, B. E. Pepa and H. Zhao, A rapid, accurate, scalable, and portable testing system for COVID-19 diagnosis, *Nat. Commun.*, 2021, **12**, 2905.

12 J. Song, *et al.*, Highly specific enrichment of rare nucleic acid fractions using Thermus thermophilus argonaute with applications in cancer diagnostics, *Nucleic Acids Res.*, 2020, **48**, e19.

13 F. Wang, *et al.*, PfAgo-based detection of SARS-CoV-2, *Biosens. Bioelectron.*, 2021, **177**, 112932.

14 G. Xun, *et al.*, Argonaute with stepwise endonuclease activity promotes specific and multiplex nucleic acid detection, *Bioresour. Bioprocess.*, 2021, **8**, 46.

15 M. Filius, *et al.*, High-Speed Super-Resolution Imaging Using Protein-Assisted DNA-PAINT, *Nano Lett.*, 2020, **20**, 2264–2270.

16 L. Chang, *et al.*, AgoFISH: cost-effective in situ labelling of genomic loci based on DNA-guided dTtAgo protein, *Nanoscale Horiz.*, 2019, **4**, 918–923.

17 A. Toudji-Zouaz, V. Bertrand and A. Barrière, Imaging of native transcription and transcriptional dynamics in vivo using a tagged Argonaute protein, *Nucleic Acids Res.*, 2021, **49**, e86.

18 S. Shin, *et al.*, Quantification of purified endogenous miRNAs with high sensitivity and specificity, *Nat. Commun.*, 2020, **11**, 6033.

19 K. S. Makarova, Y. I. Wolf, J. van der Oost and E. V. Koonin, Prokaryotic homologs of Argonaute proteins are predicted to function as key components of a novel system of defense against mobile genetic elements, *Biol. Direct*, 2009, **4**, 29.

20 S. Willkomm, K. S. Makarova and D. Grohmann, DNA silencing by prokaryotic Argonaute proteins adds a new layer of defense against invading nucleic acids, *FEMS Microbiol. Rev.*, 2018, **42**, 376–387.

21 G. Sheng, *et al.*, Structure-based cleavage mechanism of Thermus thermophilus Argonaute DNA guide strand-mediated DNA target cleavage, *Proc. Natl. Acad. Sci. U. S. A.*, 2014, **111**, 652–657.

22 L. Lisitskaya, A. A. Aravin and A. Kulbachinskiy, DNA interference and beyond: structure and functions of prokaryotic Argonaute proteins, *Nat. Commun.*, 2018, **9**, 5165.

23 Y. Wang, *et al.*, Nucleation, propagation and cleavage of target RNAs in Ago silencing complexes, *Nature*, 2009, **461**, 754–761.

24 L. Zheng, *et al.*, Loosely-packed dynamical structures with partially-melted surface being the key for thermophilic argonaute proteins achieving high DNA-cleavage activity, *Nucleic Acids Res.*, 2022, **50**, 7529–7544.

25 S. Willkomm, *et al.*, Structural and mechanistic insights into an archaeal DNA-guided Argonaute protein, *Nat. Microbiol.*, 2017, **2**, 17035.

26 S. Willkomm, *et al.*, Single-molecule FRET uncovers hidden conformations and dynamics of human Argonaute 2, *Nat. Commun.*, 2022, **13**, 3825.

27 Y. Wang, G. Sheng, S. Juranek, T. Tuschl and D. J. Patel, Structure of the guide-strand-containing argonaute silencing complex, *Nature*, 2008, **456**, 209–213.

28 P. B. Kwak and Y. Tomari, The N domain of Argonaute drives duplex unwinding during RISC assembly, *Nat. Struct. Mol. Biol.*, 2012, **19**, 145–151.

29 T. Miyoshi, K. Ito, R. Murakami and T. Uchiumi, Structural basis for the recognition of guide RNA and target DNA heteroduplex by Argonaute, *Nat. Commun.*, 2016, **7**, 11846.

30 L. Lisitskaya, *et al.*, Programmable RNA targeting by bacterial Argonaute nucleases with unconventional guide binding and cleavage specificity, *Nat. Commun.*, 2022, **13**, 4624.

31 J. W. Hegge, *et al.*, DNA-guided DNA cleavage at moderate temperatures by Clostridium butyricum Argonaute, *Nucleic Acids Res.*, 2019, **47**, 5809–5821.

32 J. S. Parker, E. A. Parizotto, M. Wang, S. M. Roe and D. Barford, Enhancement of the Seed-Target Recognition Step in RNA Silencing by a PIWI/MID Domain Protein, *Mol. Cell*, 2009, **33**, 204–214.

33 A. Zander, *et al.*, Guide-independent DNA cleavage by archaeal Argonaute from Methanocaldococcus jannaschii, *Nat. Microbiol.*, 2017, **2**, 17034.

34 E. Kaya, *et al.*, A bacterial Argonaute with noncanonical guide RNA specificity, *Proc. Natl. Acad. Sci. U. S. A.*, 2016, **113**, 4057–4062.

35 H. Dong, *et al.*, Characterization of Argonaute nucleases from mesophilic bacteria Paenibacillus borealis and Brevibacillus laterosporus, *Bioresour. Bioprocess.*, 2021, **8**, 133.

36 D. C. Swarts, *et al.*, Argonaute of the archaeon Pyrococcus furiosus is a DNA-guided nuclease that targets cognate DNA, *Nucleic Acids Res.*, 2015, **43**, 5120–5129.

37 Y. Chong, Q. Liu, F. Huang, D. Song and Y. Feng, Characterization of a recombinant thermotolerant argonaute protein as an endonuclease by broad guide utilization, *Bioresour. Bioprocess.*, 2019, **6**, 21.

38 X. Guo, *et al.*, A Hyperthermophilic Argonaute From Ferroglobus placidus With Specificity on Guide Binding Pattern, *Front. Microbiol.*, 2021, **12**, 654345.

39 R. W. Woody, "[4] Circular dichroism", in *Methods in Enzymology*, Academic Press, 1995, vol. 246, pp. 34–71.

40 F. H. Niesen, H. Berglund and M. Vedadi, The use of differential scanning fluorimetry to detect ligand interactions that promote protein stability, *Nat. Protoc.*, 2007, **2**, 2212–2221.

41 G. M. D. Ferreira, *et al.*, Lactoferrin denaturation induced by anionic surfactants: The role of the ferric ion in the protein stabilization, *Int. J. Biol. Macromol.*, 2018, **117**, 1039–1049.

42 R. P. Rambo and J. A. Tainer, Characterizing flexible and intrinsically unstructured biological macromolecules by SAS using the Porod-Debye law, *Biopolymers*, 2011, **95**, 559–571.

43 R. P. Rambo and J. A. Tainer, Super-Resolution in Solution X-Ray Scattering and Its Applications to Structural Systems Biology, *Annu. Rev. Biophys.*, 2013, **42**, 415–441.

44 K. Sharma, I. L. Antunes, V. Rajulapati and A. Goyal, Low-resolution SAXS and comparative modeling based structure analysis of endo-β-1,4-xylanase a family 10 glycoside hydrolase from Pseudopedobacter saltans comb. nov, *Int. J. Biol. Macromol.*, 2018, **112**, 1104–1114.

45 C. Putnam, Guinier peak analysis for visual and automated inspection of small-angle X-ray scattering data, *J. Appl. Crystallogr.*, 2016, **49**, 1412–1419.

46 W. E. Salomon, S. M. Jolly, M. J. Moore, P. D. Zamore and V. Serebrov, Single-Molecule Imaging Reveals that Argonaute Reshapes the Binding Properties of Its Nucleic Acid Guides, *Cell*, 2015, **162**, 84–95.

47 D. C. Swarts, *et al.*, Autonomous Generation and Loading of DNA Guides by Bacterial Argonaute, *Mol. Cell*, 2017, **65**, 985–998.e986.

48 K. W. Doxzen and J. A. Doudna, DNA recognition by an RNA-guided bacterial Argonaute, *PLoS One*, 2017, **12**, e0177097.

49 C. Wang, D. A. Greene, L. Xiao, R. Qi and R. Luo, Recent Developments and Applications of the MMPBSA Method, *Front. Mol. Biosci.*, 2018, **4**, 87.

50 J. Li, X. Zhang, L. Hong and Y. Liu, Entropy Driving the Mg^{2+}-Induced Folding of TPP Riboswitch RNA, *J. Phys. Chem. B*, 2022, **126**, 9457–9464.

51 J. L. Fiore, E. D. Holmstrom and D. J. Nesbitt, Entropic origin of Mg^{2+}-facilitated RNA folding, *Proc. Natl. Acad. Sci. U. S. A.*, 2012, **109**, 2902–2907.

52 H. Son, *et al.*, Mg^{2+}-dependent conformational rearrangements of CRISPR-Cas12a R-loop complex are mandatory for complete double-stranded DNA cleavage, *Proc. Natl. Acad. Sci. U. S. A.*, 2021, **118**, e2113747118.

53 C. Andreini, I. Bertini, G. Cavallaro, G. L. Holliday and J. M. Thornton, Metal ions in biological catalysis: from enzyme databases to general principles, *JBIC, J. Biol. Inorg. Chem.*, 2008, **13**, 1205–1218.

54 C. Hureau and P. Faller, Aβ-mediated ROS production by Cu ions: Structural insights, mechanisms and relevance to Alzheimer's disease, *Biochimie*, 2009, **91**, 1212–1217.

55 F. H. Yu and W. A. Catterall, The VGL-Chanome: A Protein Superfamily Specialized for Electrical Signaling and Ionic Homeostasis, *Sci. STKE*, 2004, re15.

56 Y. Nevo and N. Nelson, The NRAMP family of metal-ion transporters, *Biochim. Biophys. Acta, Mol. Cell Res.*, 2006, **1763**, 609–620.

57 B. P. Kleinstiver, *et al.*, Engineered CRISPR–Cas12a variants with increased activities and improved targeting ranges for gene, epigenetic and base editing, *Nat. Biotechnol.*, 2019, **37**, 276–282.

58 M. H. Tran, *et al.*, A more efficient CRISPR-Cas12a variant derived from Lachnospiraceae bacterium MA2020, *Mol. Ther.–Nucleic Acids*, 2021, **24**, 40–53.

59 D. Svergun, C. Barberato and M. H. J. Koch, CRYSOL - a Program to Evaluate X-ray Solution Scattering of Biological Macromolecules from Atomic Coordinates, *J. Appl. Crystallogr.*, 1995, **28**, 768–773.

60 D. I. Svergun, M. V. Petoukhov and M. H. J. Koch, Determination of Domain Structure of Proteins from X-Ray Solution Scattering, *Biophys. J.*, 2001, **80**, 2946–2953.

61 K. Manalastas-Cantos, *et al.*, ATSAS 3.0: expanded functionality and new tools for small-angle scattering data analysis, *J. Appl. Crystallogr.*, 2021, **54**, 343–355.

62 D. Franke, *et al.*, ATSAS 2.8: a comprehensive data analysis suite for small-angle scattering from macromolecular solutions, *J. Appl. Crystallogr.*, 2017, **50**, 1212–1225.

63 J. Jumper, *et al.*, Highly accurate protein structure prediction with AlphaFold, *Nature*, 2021, **596**, 583–589.

64 J. Huang, *et al.*, CHARMM36m: an improved force field for folded and intrinsically disordered proteins, *Nat. Methods*, 2017, **14**, 71–73.

65 B. Hess, C. Kutzner, D. van der Spoel and E. Lindahl, GROMACS 4: Algorithms for Highly Efficient, Load-Balanced, and Scalable Molecular Simulation, *J. Chem. Theory Comput.*, 2008, **4**, 435–447.

66 U. Essmann, *et al.*, A smooth particle mesh Ewald method, *J. Chem. Phys.*, 1995, **103**, 8577–8593.

67 G. Bussi, D. Donadio and M. Parrinello, Canonical sampling through velocity rescaling, *J. Chem. Phys.*, 2007, **126**, 014101.

68 M. Parrinello and A. Rahman, Polymorphic transitions in single crystals: A new molecular dynamics method, *J. Appl. Phys.*, 1981, **52**, 7182–7190.

69 Y. Wang, *et al.*, Structure of an argonaute silencing complex with a seed-containing guide DNA and target RNA duplex, *Nature*, 2008, **456**, 921–926.

70 Y. Liu, *et al.*, A programmable omnipotent Argonaute nuclease from mesophilic bacteria Kurthia massiliensis, *Nucleic Acids Res.*, 2021, **49**, 1597–1608.

71 Y. Cao, *et al.*, Argonaute proteins from human gastrointestinal bacteria catalyze DNA-guided cleavage of single-and double-stranded DNA at 37° C, *Cell discovery*, 2019, **5**, 38.

72 L. Wang, *et al.*, A bacterial Argonaute with efficient DNA and RNA cleavage activity guided by small DNA and RNA, *Cell Rep.*, 2022, **41**, 111533.

73 X. Jiang, Y. Liu, Q. Liu and L. Ma, Characterization of a Programmable Argonaute Nuclease from the Mesophilic Bacterium Rummeliibacillus suwonensis, *Biomolecules*, 2022, **12**, 355.

74 Q. Liu, *et al.*, A programmable pAgo nuclease with RNA target-cleavage specificity from the mesophilic bacterium Verrucomicrobia: A pAgo with RNA target cleavage specificity, *Acta Biochim. Biophys. Sin.*, 2023, **55**, 1204.